Ion Coulomb Crystals With Long Range Order in RF-traps

Anders Mortensen[*], Esben Nielsen[*], Thierry Matthey[†], Jan Petter Hansen[**] and Michael Drewsen[*]

[*]*QUANTOP – Danish National Research Foundation Center for Quantum Optics, Department of Physics and Astronomy, University of Aarhus, 8000 Aarhus, Denmark*
[†]*Parallab, Department of Informatics, P.O. Box 7800, University of Bergen, 5007 Bergen, Norway*
[**]*Department of Physics, P.O. Box 7800, University of Bergen, 5007 Bergen, Norway*

Abstract. In this contribution, we present results on the structural properties of single-component as well as two-component ion Coulomb crystals confined in a linear Paul trap. Metastable long range ordered structures as the face-centered cubic (fcc) and body-centered cubic (bcc) lattices are observed in single-component ion crystals of sizes down to ~ 1000 ions. In the case of two-component ion crystals we observe a stable long range ordered structure in one of the trapped components, which is compared with a Molecular Dynamics (MD) simulation of a two-component crystal.

PACS: 32.80.Pj, 52.27.Jt, 52.27.Gr, 36.40.Ei

INTRODUCTION

When confined ions with the same sign of charge are cooled to mK temperatures they form a solid state called the ion Coulomb crystal. Ion Coulomb crystals have been realized with laser cooled ions in Penning and Paul traps for more than a decade and are excellent targets for studying size effects of finite one-component plasmas [1–10]. While the predicted ground state structure of infinite one-component ion plasmas is bcc [11], i.e. a 3D long range ordered structure, the structures of finite ion Coulomb crystals are much more diverse. Previously long range order structures, like the bcc and fcc lattices, have been studied in larger ion Coulomb crystals consisting of more than 50,000 ions trapped in Penning traps [2, 3, 8]. In smaller ion crystals, where surface effects dominate, the structures are determined by the boundary conditions set by the trapping potentials and long range order is not necessarily present. In our experiment Ca^+ ions are trapped in an linear Paul trap where the ions are confined by rf electric fields.

THE LINEAR PAUL TRAP

The linear Paul trap used in these experiments consists of four cylindrical electrode rods in a quadrupole configuration as shown in Fig. 1. The electrodes have radii of 4.00 mm and the inter-electrode spacing is $r_0 = 3.5$ mm. A harmonically driven quadrupole electric field between the rods is obtained by applying a time varying voltage $\frac{1}{2}U_{\rm rf}\cos(\Omega_{\rm rf}t)$ to two diagonally opposite electrodes and a voltage with the opposite

CP862, *Non-Neutral Plasma Physics VI, Workshop on Non-Neutral Plasmas 2006,*
edited by M. Drewsen, U. Uggerhøj, and H. Knudsen

phase $\frac{1}{2}U_{\rm rf}\cos(\Omega_{\rm rf}t+\pi)$ to the two neighboring electrode rods. While this confines the ions radially, i.e. in the *xy*-plane, axial confinement along the *z*-axis is accomplished by a sectioning of each of the electrode rods into three pieces and then applying a static bias voltage $U_{\rm end}$ to the end-electrodes. The length of the center-electrode is $2z_0 = 5.4$ mm and the length of the end-electrodes is 20 mm. The quadrupole electric field is operated at frequency $\Omega_{\rm rf} = 2\pi \times 3.88$ MHz and trap parameters in the present experiments are $U_{\rm rf} \sim 400$–540 V and $U_{\rm end} \sim 10$–50 V. In the approximation that a time-average of the fast oscillating ion motion in the harmonically driven electric field is made the resulting ion confinement is well described by a harmonic pseudo potential $\Phi_{\rm ps}(r,z) = \frac{1}{2}m(\omega_r^2 r^2 + \omega_z^2 z^2)$, where ω_r and ω_z are the radial and axial trap frequencies, respectively [5], and m is the ion mass. The zero-temperature ion density is in the pseudopotential approximation given by $n_{\rm theo} = \varepsilon_0 U_{\rm rf}^2/mr_0^4\Omega_{\rm rf}^2$, where ε_0 is the vacuum permittivity.

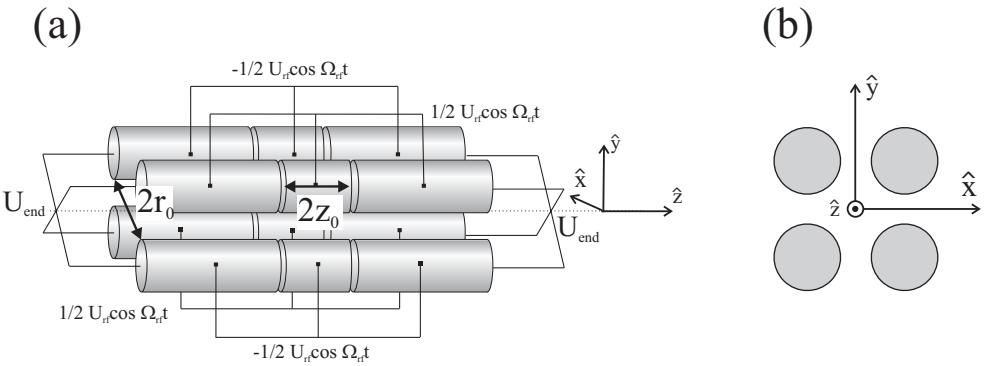

FIGURE 1. (a) Linear Paul trap electrode configuration with applied voltages. (b) End-view of the Paul trap with the definitions of the $\hat{x}$ and $\hat{y}$ axis.

PRODUCTION AND DETECTION OF ION CRYSTALS

The Ca^+ ions are produced isotope selectively in the center of the linear Paul trap by two photon resonance enhanced photo-ionization of an effusive beam of naturally abundant calcium [12, 13]. The trapped Ca^+ ions are then Doppler laser cooled by applying the cooling lasers along the trap axis (*z*-axis). The optical transitions used for the Doppler laser cooling are depicted in Fig. 2(a). The main cooling transition is from the $4S_{1/2}$ ground state to the $4P_{1/2}$ state at 397 nm. To avoid shelving in the metastable $3D_{3/2}$ state we apply repump lasers. Repumping is done either via the $4P_{1/2}$ state using an 866 nm laser or via the $4P_{3/2}$ state using two repump lasers at 850 nm and 854 nm. Laser light at 397 nm is produced by a Ti:sapph laser or a diode laser and the three wavelengths in the infrared (850 nm, 854 nm, and 866 nm) are covered by diode lasers.

The positions of the trapped and cooled ions are imaged by an image intensified CCD camera placed above the trap, which detects the 397 nm light which is spontaneously emitted when the ions are Doppler laser cooled. Only ions that are Doppler laser cooled during the exposure period of the camera are accordingly visible in the images. The

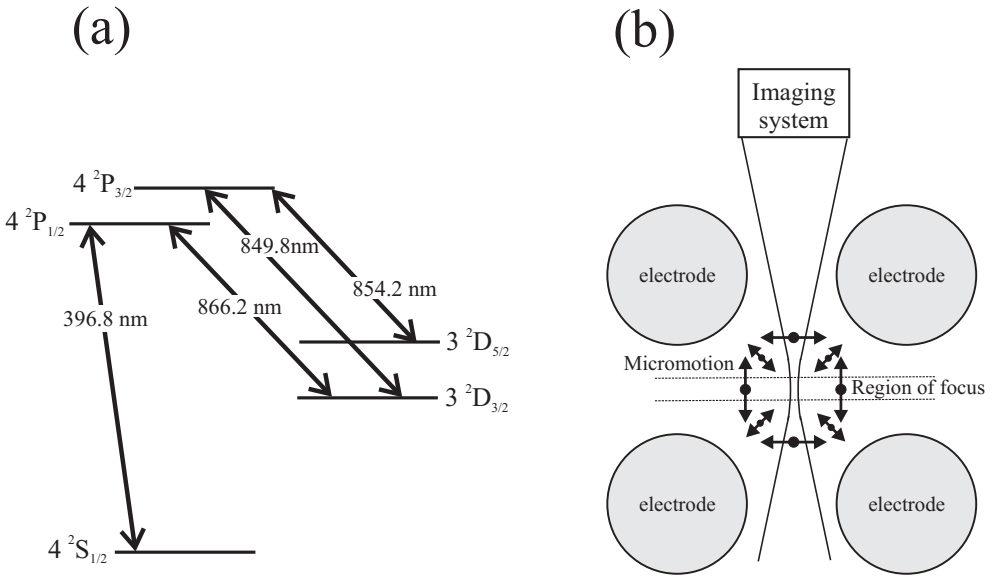

FIGURE 2. (a) Optical transitions for Doppler laser cooling of Ca^+ ions. (b) Illustration of the direction of the micromotion at different positions in the ion crystal.

camera system is also equipped with a 14× magnification system which corresponds to a resolution of 0.71 μm/pixel in the images.

Because the ions are confined by a quadrupole rf-field they perform a fast oscillating motion called the micromotion. The direction and amplitude of the micromotion which is illustrated in Fig. 2(b) is position dependent and thus only ions closest to the image plane of the camera system move in parallel to the direction of view of the camera system (see Ref. [6]). Furthermore the exposure time of the camera system is 100 ms so many rf-cycles of the ion motion are averaged in each image. The ions near the image plane thus appear as bright point-like features in the images if the crystal structure is stable during the image acquisition, while other ions that are both out of focus and have a component of the micromotion perpendicular to the direction of view contribute with a blurred background in the images.

NEAR SPHERICAL SINGLE-COMPONENT ION COULOMB CRYSTALS

We have performed a series of measurements on near spherical ion Coulomb crystals consisting of $^{40}Ca^+$ ions. Figure 3 shows images of ion crystals in the range 300–1700 ions trapped at an rf-voltage $U_{rf} \approx 400$ V. The images in Figs. 3(a)–3(c) show instants where the projection of the ion positions form ringlike structures, which indicates that during the exposure time of these images the ions are localized in concentric near-spherical shells. This is the type of crystal structure which has been predicted by Hasse

et.al. [14] for spherical ion crystals of sizes below ~ 5000 ions. Figure 3(d)– 3(f) are images of the same ion ensembles, but at instants where the ions have arranged such that the projection images become hexagonal. From a density point of view as well as from the fact that the depth of focus is $\sim 50\ \mu$m, which is several times the Wigner Seitz radius ($\sim 10\ \mu$m), we can conclude that the observed hexagonal projection must originate from more than one layer of ions. The observed hexagonal projections can therefore not be a two-dimensional structure and consequently the ions must have arranged in a three dimensional long range ordered structure.

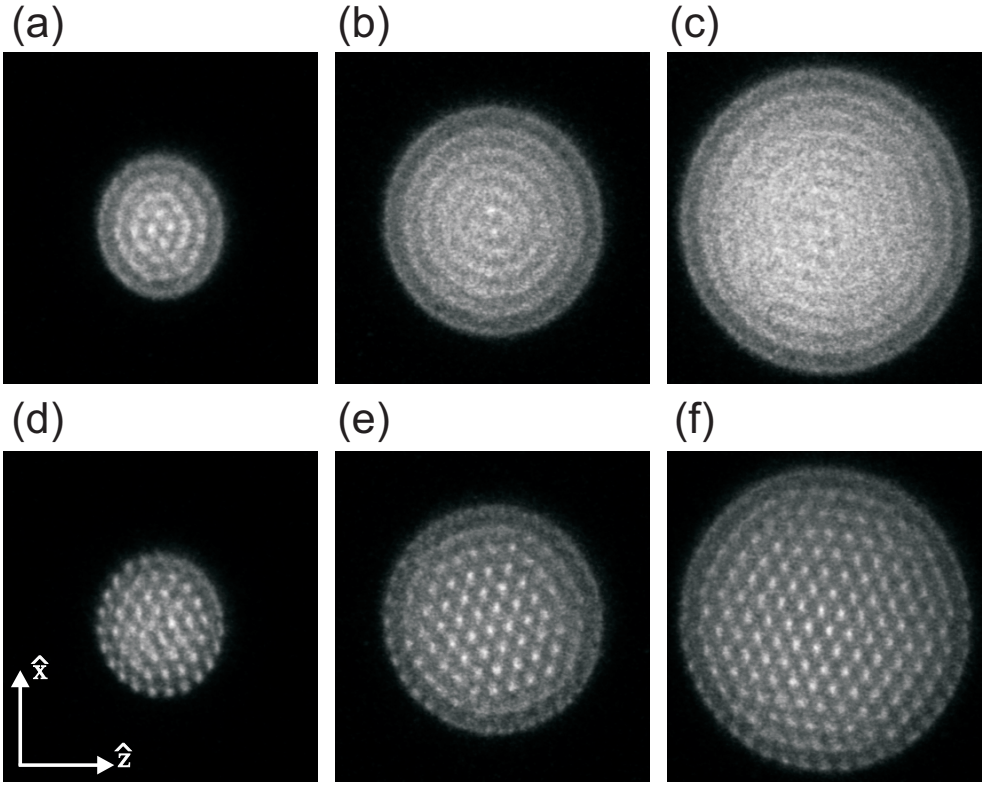

FIGURE 3. Images of near spherical crystals showing both concentric shell structures (a)–(c) and long range ordered structures (d)–(f). The ion crystals contain about 300 ions ((a) & (d)), 770 ions ((b) & (e))), and 1700 ions ((c) & (f)). The width of each image is about 250 μm.

The bcc structure is a good candidate for a three dimensional structures that give rise the observed hexagonal projection as this is the ground state structure of infinite one component ion systems [11]. Actually a bcc structure viewed along the [111]-direction gives rise to a hexagonal projection as the observed. The ion density calculated from the assumption that the observed structure is indeed a bcc structure observed along the [111]-direction is $n_{bcc} = (2.1 \pm 0.3) \times 10^8$ cm^{-3} in perfect agreement with the ion density calculated from the trap parameters $n_{\text{theo}} = (2.3 \pm 0.2) \times 10^8$ cm^{-3} using the formula for n_{theo} (See Sect. THE LINEAR PAUL TRAP). The other cubic structures sc

and fcc also gives rise to a hexagonal projection when viewed along the [111]-direction, but these can be excluded as the observed ion density would be off by a factor of two or more from the predicted (see [6]). This strongly supports that the observed structure is indeed a bcc structure.

MD simulations have indicated that the ground state structure of spherical ion Coulomb crystals only show distinct bcc structure when the ion numbers exceed ~ 5000 [15, 16]. To understand why we nevertheless observe bcc structures in smaller crystals we have performed MD simulations where a certain fraction of the ions in the center of the ion Coulomb crystal have been fixed in a bcc structure and the other ions are allowed to relax. The results of the MD simulations have been presented in Ref. [6], and they show that the excess potential energy of such structures is much smaller than the thermal energy of the ion crystal. Furthermore by subsequently releasing the fixed ions and slowly heating the ions to a few mK in the simulation indicates that the bcc structures could be metastable on the timescale of the exposure time of the camera (~ 100 ms).

When the number of ions in the ion Coulomb crystals exceeds ~ 2000 there are indications that long range ordered structures other than the bcc structure might occur. An example of this is seen in Fig. 4 where two images of a slightly prolate ion crystals containing about 13,000 ions are shown. The Paul trap is operated at $U_{\mathrm{rf}} \approx 400$ V, which gives an ion density of $n_{\mathrm{theo}} = (2.2 \pm 0.2) \times 10^8$ cm^{-3}. In the first image (Fig. 4(a)) the ions are arranged such that they give a hexagonal projection and from an ion density point of view we can, as in the previous example, conclude that a bcc structure viewed along the [111]-direction would give rise to this projection. In the second image, (Fig. 4(b)) the projection of the underlying long range ordered structure gives rise to a rectangular lattice in the image. The observed height and width of each rectangle in the lattice are $h_{\mathrm{obs}} = 15.2 \pm 0.5$ μm and $w_{\mathrm{obs}} = 9.7 \pm 0.2$ μm, respectively. Among the cubic lattices we find that the fcc lattice viewed along the [211] direction have a similar rectangular projection. Indeed, if we assume that it is an fcc [211] with ion density $n_{\mathrm{theo}} = (2.2 \pm 0.2) \times 10^8$ cm^{-3} the height and width of the rectangles in the projection image would be $h_{\mathrm{theo}} = 15.2 \pm 0.5$ μm and $w_{\mathrm{theo}} = 9.3 \pm 0.3$ μm.

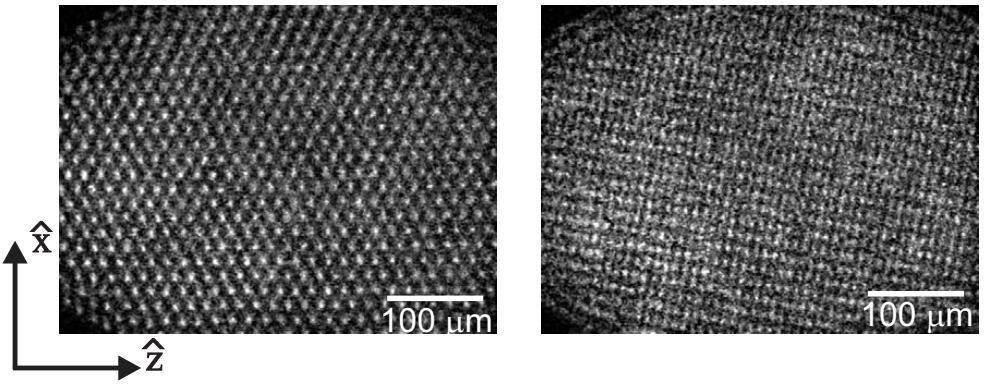

FIGURE 4. Images of an ion crystal containing $\sim 13,000$ ions. The long range ordered structure projections are identified as bcc [111] and fcc [211] structures.

TWO-COMPONENT ION COULOMB CRYSTALS

In this section we describe our studies on the structures of ion Coulomb crystals consisting of two different isotopes of the Ca^+ ion, namely $^{40}Ca^+$ and $^{44}Ca^+$ ions. In ion crystals having two components with the same charge, but different mass, the two ion components are completely radially separated because the linear Paul trap exert a mass dependent radial confinement force on the ions, while axial confinement is independent of the ion mass. In the case of the two-component ion Coulomb crystals we study, also called bicrystals, this means that the lighter isotope ($^{40}Ca^+$) is situated as a cylindrical core surrounded by the heavier isotope ($^{44}Ca^+$). In this section we present observations of long range ordered structure in the $^{40}Ca^+$ part of the crystal and in contrast to the long range ordered structure observed in the one-component case this structure is very stable.

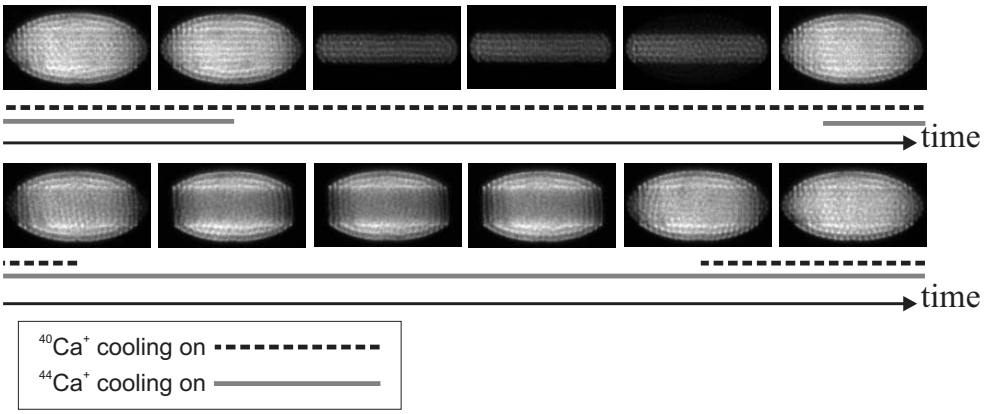

FIGURE 5. Image sequence showing the alternating cooling of $^{40}Ca^+$ and $^{44}Ca^+$ ions. The crystal contains about 500 $^{40}Ca^+$ ions and 1400 $^{44}Ca^+$ ions. The image acquisition rate is $\sim$ 6 Hz and $U_{rf} \approx 400$ V.

The bicrystals are loaded by resonant isotope selective photo-ionization of ^{44}Ca atoms. Subsequently we can convert a desired number of the $^{44}Ca^+$ ions into $^{40}Ca^+$ ions by near-resonant electron transfer collisions with atoms in the effusive atomic beam of naturally abundant calcium containing 96.9% ^{40}Ca atoms for a controlled period of time. Due to the isotope shifts of the cooling transitions [17, 18], each isotope requires its own set of laser cooling frequencies. Because we want to image both isotopes we apply two sets of cooling lasers, one for each isotope ion. For Doppler laser cooling of $^{40}Ca^+$ ions we use 397 nm, 850 nm, and 854 nm diode lasers and for the $^{44}Ca^+$ ions we use a 397 nm frequency doubled Ti:Sapphire laser together with an 866 nm diode laser. The advantage of using two sets of laser systems is that we can independently turn of Doppler laser cooling of each isotope and in this way distinguish between the isotopes, since the ions are only fluorescing when they are directly laser cooled. A sequence of images showing alternating cooling of $^{40}Ca^+$ and $^{44}Ca^+$ is shown in Fig. 5. The cooling sequence was made alternating by blocking and un-blocking the 850 nm laser ($^{40}Ca^+$ laser cooling off) and the 866 nm laser ($^{44}Ca^+$ laser cooling off) using mechanical shutters at a repetition rate of $\sim$ 1 Hz. Due to sympathetic cooling [19, 20] of the component which is not

directly laser cooled at a given time, the full ion Coulomb crystal retains its structure and shape during this alternating cooling sequence, and as seen in Fig. 5 show the lightest isotope, $^{40}Ca^+$, is located closest to the trap axis as a cylindrical core surrounded by the heavier $^{44}Ca^+$ ions.

In this contribution we will focus on the bulk structural properties of the $^{40}Ca^+$ ion core of $^{40}Ca^+$–$^{44}Ca^+$ bicrystals similar to those in Fig. 5. In Fig. 6 a sequence images of the $^{40}Ca^+$ core is shown. The trap potential is $U_{\rm rf} \approx 540$ V, while the end cap voltage is varied. The image sequence in Fig. 6 illustrates how the ion Coulomb crystal shape and structure change as the trap parameter $U_{\rm end}$ is varied. It shows that despite the changes in the outer shape of the $^{40}Ca^+$ core the rectangular lattice in the projection of the ions is preserved in all four images, which indicate that the observed long range ordered structure is rather stable to changes in the boundary conditions of the crystal shape. From the images in Fig. 6 we immediately see that the projection of the structure is a 2D rectangular lattice which is aligned with respect to the trap axis. Since again the depth of focus of the imaging system ($\sim$50 μm) is several times the inter-ion distance, the observed projection must originate from some layers of ions, i.e. to obtain the rectangular structure in this image the ions must have arranged with a 3D long range ordering. No observations of transitions to other projection structures were made during the data acquisition which leads us to infer that the observed 3D long range order is very stable. The temporal stability and the orientational alignment of the long range ordered structure are distinctly different from observations of metastable long range order in spherical one-component ion crystals, which was described previously in this contribution. Accordingly, we conclude that the presence of the surrounding $^{44}Ca^+$ ions has a great impact on the formation and appearance of the observed long range ordered structure in the $^{40}Ca^+$ part of the crystal.

To get an understanding of why we see these long range ordered structures in the $^{40}Ca^+$ core of the bicrystal we made a series of MD simulations. MD simulations that utilize a pseudopotential, i.e.,

$$\Phi_{\rm ps}(r,z) = \frac{1}{2}M(\omega_r^2 r^2 + \omega_z^2 z^2), \tag{1}$$

did not predict a long range ordered structure in bulk of the ion crystal. So consequently we instead turned to the full time dependent electric potential

$$\phi_{\rm tot}(x,y,z,t) = -\frac{1}{2}U_{\rm rf}\cos\Omega_{\rm rf}t\,\frac{2xy}{r_0^2} - \frac{1}{2}\eta U_{\rm end}\frac{x^2+y^2-2z^2}{z_0^2}, \tag{2}$$

to simulate the crystal structure. Here $\eta = 0.248$ is a geometrical constant specific for our trap. Such a simulation of a crystal that contains 1509 $^{40}Ca^+$ ions and 1979 $^{44}Ca^+$ ions is shown in Fig. 7. In Fig. 7(a)– 7(c) we have shown the end-view of the crystal which is a projection of all the ion positions onto the *xy* plane. Closest to the trap axis the ions have lined up in four rows and four columns which indicate that the simulation predicts that there is a long range ordered structure in the bulk of the $^{40}Ca^+$ core of the crystal. Furthermore this long range ordered structure is oriented with respect to the major linear Paul trap axis ($\hat{x}$, $\hat{y}$ and $\hat{z}$- axis). This indicates that the micromotion of the ions plays a role in the orientation of this structure.

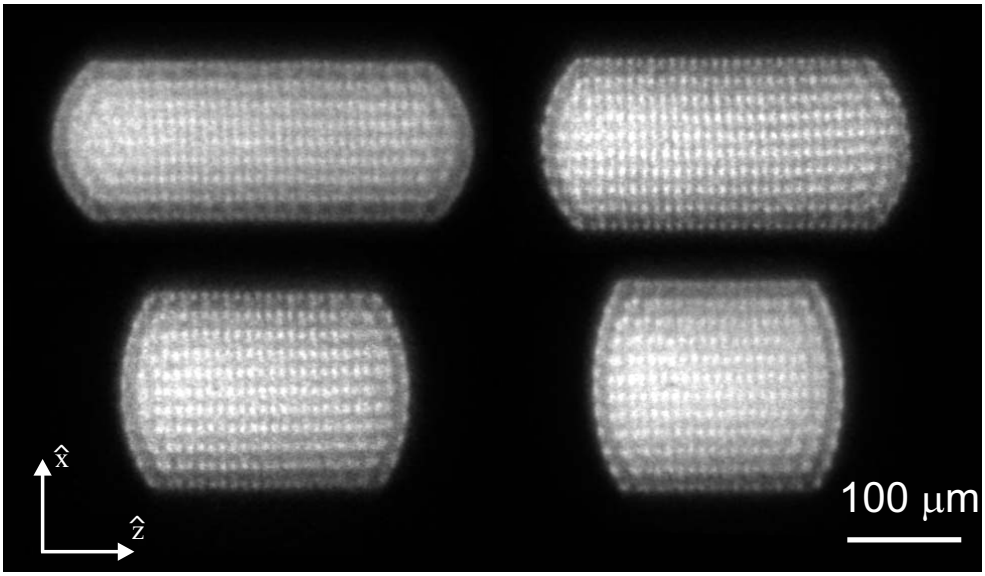

FIGURE 6. The $^{40}Ca^{+}$ ion part of a bicrystal that contains $\sim$1500 $^{40}Ca^{+}$ ions and $\sim$2000 $^{44}Ca^{+}$ ions. The $^{44}Ca^{+}$ part of the crystal is not visible in these images.

A visual comparison between the simulation and our data shown in Fig. 6 is accomplished by projecting the positions of the $^{40}Ca^{+}$ ions that are closest to the plane spanned by $\hat{x}$ and $\hat{z}$ (see Fig. 1). More precisely the $^{40}Ca^{+}$ ions included in the projection is situated between the dotted lines in Fig. 7(b) (separation 34 μm). The resulting projection is seen in Fig. 7(d) where it is clear that the simulation predicts a rectangular projection of the ions similar to the observed data in Fig. 6.

A careful analysis of the simulated data reveals an organization of the $^{40}Ca^{+}$ ions ion a face-centered tetragonal (fct) lattice. A projection of the lattice structure, which corresponds to the view of our camera system, gives a rectangular projection that has a height to width ratio of $h_{\mathrm{fct}}/w_{\mathrm{fct}} = \sqrt{3} \simeq 1.73$. Experimentally we observe a height to width ratio of the rectangles of $h_{\mathrm{obs}}/w_{\mathrm{obs}} = 1.62 \pm 0.07$. Interestingly this latter ratio is in better agreement with an fcc lattice viewed along the [211] direction, which has a rectangular projection with a height to width ratio $h_{\mathrm{fcc}}/w_{\mathrm{fcc}} \simeq 1.63$. In Tab. 1 the observed height and width of the rectangular structure is compared with the height and width that can be calculated from the assumption that the ion density is $n_{\mathrm{theo}} = (4.3 \pm 0.3) \times 10^{8}$ cm^{-3} and the assumption that the projection originates either from an fct lattice of an fcc lattice. As seen from Tab. 1 these numbers does not bring us closer to a conclusion on whether the ions actually arrange in an fcc lattice or an fct lattice, but together with the fact that the height to width ratio is only consistent with an fcc lattice we tend to conclude that the ions are arranged in a possibly slightly distorted fcc lattice and viewed along the [211]-direction.

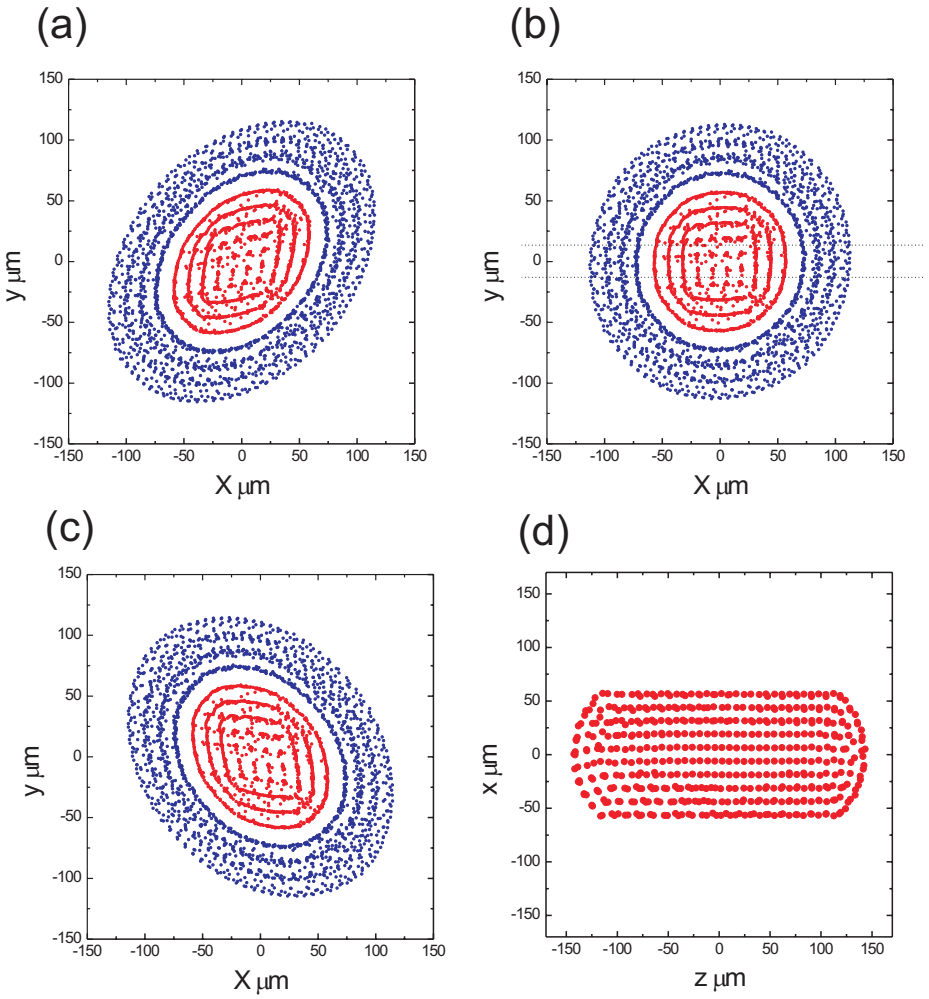

FIGURE 7. (a)–(c) Projection in the xy-plane of a simulated two-component crystal containing 1509 $^{40}Ca^{+}$ ions and 1979 $^{44}Ca^{+}$ ions. The three projections show the ion crystal at different stages of the micromotion when $\Omega_{\mathrm{rf}}t = 2\pi N$ (a), $\Omega_{\mathrm{rf}}t = 2\pi N + \pi/2$ (b), and $\Omega_{\mathrm{rf}}t = 2\pi N + \pi$ (c). Fig. (d) shows a projection onto the *xz*-plane of positions of all the $^{40}Ca^{+}$ ions that are located between the dotted lines in Fig. (b).

ACKNOWLEDGMENTS

We acknowledge financial support from the Carlsberg Foundation.

TABLE 1. Observed height and width of the rectangular projected structure compared with the height and width calculated assuming an fct and an fcc structure if the ion density is $n_{\text{theo}} = (4.3 \pm 0.3) \times 10^8\,\text{cm}^{-}3$.

	Observation	**Assuming fct (simulation)**	**Assuming fcc[211]**
h [μm]	12.6 ± 0.3	12.8 ± 0.3	12.2 ± 0.3
w [μm]	7.8 ± 0.3	7.4 ± 0.2	7.5 ± 0.3

REFERENCES

1. G. Birkl, S. Kassner, and H. Walther, *Nature* **357**, 310–313 (1992).
2. T. B. Mitchell, J. J. Bollinger, D. H. E. Dubin, X.-P. Huang, W. M. Itano, and R. H. Baughman, *Science* **282**, 1290–1293 (1998).
3. W. M. Itano, J. J. Bollinger, J. N. Tan, B. Jelenković, X.-P. Huang, and D. J. Wineland, *Science* **279**, 686–689 (1998).
4. M. Drewsen, C. Brodersen, L. Hornekær, J. S. Hangst, and J. P. Schiffer, *Phys. Rev. Lett.* **81**, 2878 (1998).
5. L. Hornekær, N. Kjærgaard, A. M. Thommesen, and M. Drewsen, *Phys. Rev. Lett.* **86**, 1994 (2001).
6. A. Mortensen, E. Nielsen, T. Matthey, and M. Drewsen, *Phys. Rev. Lett.* **96**, 103001 (2006).
7. T. Schätz, U. Schramm, and D. Habs, *Nature* **412**, 717–720 (2001).
8. J. N. Tan, J. J. Bollinger, B. Jelenkovic, and D. J. Wineland, *Phys. Rev. Lett.* **75**, 4198–4201 (1995).
9. N. Kjærgaard, and M. Drewsen, *Phys. Rev. Lett.* **91**, 095002 (2003).
10. R. Blümel, J. M. Chen, E. Peik, W. Quint, W. Schleich, Y. R. Shen, and H. Walther, *Nature* **334**, 309–313 (1988).
11. S. G. Brush, H. L. Sahlin, and E. Teller, *J. Chem. Physics* **45**, 2102–2118 (1966).
12. N. Kjærgaard, L. Hornekær, A. Thommesen, Z. Videsen, and M. Drewsen, *Appl. Phys. B* **71**, 207–210 (2000).
13. A. Mortensen, J. J. T. Lindballe, I. S. Jensen, P. Staanum, D. Voigt, and M. Drewsen, *Phys. Rev. A* **69**, 042502 (2004).
14. R. W. Hasse, and V. V. Avilov, *Phys. Rev. A* **44**, 4506–4515 (1991).
15. H. Totsuji, T. Kishimoto, C. Totsuji, and K. Tsuruta, *Phys. Rev. Lett.* **88**, 125002 (2002).
16. R. W. Hasse, *J. Phys. B* **36**, 1011–1017 (2003).
17. A.-M. Mårtensson-Pendrill, A. Ynnerman, H. Warston, L. Vermeeren, R. E. Silverans, A. Klein, R. Neugart, C. Schulz, P. Lievens, and The ISOLDE Collaboration, *Phys. Rev. A* **45**, 4675–4681 (1992).
18. W. Alt, M. Block, V. Schmidt, T. Nakamura, P. Seibert, X. Chu, and G. Werth, *J. Phys. B* **30**, L677–L681 (1997).
19. P. Bowe, L. Hornekær, C. Brodersen, M. Drewsen, J. S. Hangst, and J. P. Schiffer, *Phys. Rev. Lett.* **82**, 2071 (1999).
20. D. J. Larson, J. C. Bergquist, J. J. Bollinger, W. M. Itano, and D. J. Wineland, *Phys. Rev. Lett.* **57**, 70–73 (1986).